

1 **Intensive photochemical oxidation in the marine atmosphere:**

2 **Evidence from direct radical measurements**

3 Guoxian Zhang^{1,2}, Renzhi Hu^{1,*}, Pinhua Xie^{1,2,3, **}, Changjin Hu¹, Xiaoyan Liu⁴,

4 Liujun Zhong¹, Haotian Cai¹, Bo Zhu⁵, Shiyong Xia⁵, Xiaofeng Huang⁵, Xin Li⁶,

5 Wenqing Liu¹

6 ¹ Key Laboratory of Environment Optics and Technology, Anhui Institute of Optics and Fine
7 Mechanics, HFIPS, Chinese Academy of Sciences, Hefei, China

8 ² University of Science and Technology of China, Hefei, China

9 ³ College of Resources and Environment, University of Chinese Academy of Science, Beijing,
10 China

11 ⁴ School of Pharmacy, Anhui Medical University, Hefei, China

12 ⁵ Key Laboratory for Urban Habitat Environmental Science and Technology, School of
13 Environment and Energy, Peking University Shenzhen Graduate School, Shenzhen, China

14 ⁶ State Key Joint Laboratory of Environmental Simulation and Pollution Control, College of
15 Environmental Sciences and Engineering, Peking University, Beijing, China

16
17 ***Correspondence to:** Renzhi Hu, Key Laboratory of Environment Optics and
Technology, Anhui Institute of Optics and Fine Mechanics, HFIPS, Chinese Academy
18 of Sciences, Hefei, China

19
20 ****Correspondence to:** Pinhua Xie, University of Science and Technology of China,
Hefei, China

21
22 **Email addresses:** rzhu@aiofm.ac.cn (Renzhi Hu); phxie@aiofm.ac.cn (Pinhua Xie)

24 **Abstract:** Comprehensive observations of hydroxyl (OH) and hydroperoxy (HO₂)
25 radicals were conducted in October 2019 at a coastal continental site in the Pearl
26 River Delta (YMK site, 22.55°N, 114.60°E). The daily maximum OH and HO₂
27 concentrations were $(4.7\text{--}9.5) \times 10^6 \text{ cm}^{-3}$ and $(4.2\text{--}8.1) \times 10^8 \text{ cm}^{-3}$, respectively. The
28 synchronized air mass transport from the northern cities and the South China Sea
29 exerted a time-varying influence on atmospheric oxidation. Under a typical ocean-
30 atmosphere (OCM), reasonable measurement model agreement was achieved for both
31 OH and HO₂ using a 0-D chemical box model incorporating the regional atmospheric
32 chemistry mechanism version 2-Leuven isoprene mechanism (RACM2-LIM1), with
33 daily averages of $4.5 \times 10^6 \text{ cm}^{-3}$ and $4.9 \times 10^8 \text{ cm}^{-3}$, respectively. Land mass (LAM)
34 influence promoted more active photochemical processes, with daily averages of 7.1
35 $\times 10^6 \text{ cm}^{-3}$ and $5.2 \times 10^8 \text{ cm}^{-3}$ for OH and HO₂, respectively. Heterogeneous uptake
36 had certain effects on HO_x chemistry, but the influence of the halogen mechanism
37 was limited by NO_x level. Intensive photochemistry occurred after precursor
38 accumulation, allowing local net ozone production comparable with surrounding
39 suburban environments (5.52 ppb/h during the LAM period). Rapid oxidation process
40 was accompanied by a higher diurnal nitrous acid (HONO) concentration ($> 400 \text{ ppt}$).
41 After a sensitivity test, HONO-related chemistry elevated the ozone production rate
42 by 33% and 39% during the LAM and OCM periods, respectively. The nitric acid
43 (P(HNO₃)) and sulfuric acid (P(H₂SO₄)) formation rates also increased
44 simultaneously (~43% and ~48% for LAM and OCM sectors, respectively). In the
45 ozone-prediction test, simulated O₃ decreased from ~75 ppb to a global background
46 (~35 ppb) without the HONO constraint, and daytime HONO concentrations were
47 reduced to a low level (~70 ppt). For coastal cities, the particularity of the HONO
48 chemistry tends to influence the ozone-sensitive system and eventually magnifies the
49 background ozone. Therefore, the promotion of oxidation by elevated precursors
50 deserves a lot of attention when aiding pollution mitigation policies.

51 **Keywords:** FAGE-LIF; OH and HO₂ radicals; Atmospheric oxidation; Marine
52 boundary layer; Precursors;

53 1 Introduction

54 The marine boundary layer (MBL) occupies 71% of the planetary boundary layer,
55 is a massive active carbon sink on Earth, and plays an irreplaceable role in coping
56 with global climate change (Stone et al., 2012; Woodward-Massey et al., 2022b; Liu
57 et al., 2022a). As a typical background atmosphere on the Earth, the MBL is
58 equivalent to a natural smog chamber with limited anthropogenic emissions and is
59 characterized by low NO_x (the sum of nitric oxide (NO) and nitrogen dioxide (NO₂))
60 and non-methane hydrocarbons (NMHCs) under a layer of clean air (Woodward-
61 Massey et al., 2022b). The lifetime of OH radical, a key oxidant, is on the order of a
62 few hundred milliseconds (Fuchs et al., 2012). Due to the scarcity of oxidation
63 precursors, including nitrous acid (HONO), formaldehyde (HCHO), and NMHCs, the
64 reaction between O¹D and water vapor generally dominates the radical initiation
65 pathway in the marine environment. For example, in a tropical boundary layer
66 observation experiment (reactive halogens in the marine boundary layer, RHaMBLe),
67 ozone photolysis was found to account for 70% of the OH radical source based on the
68 master chemical mechanism (MCM) (Whalley et al., 2010). The vital role of ozone
69 photolysis is contrasting with typical polluted and semi-polluted areas investigated in
70 a series of field campaigns, in which the propagation routes were found to dominate
71 the radical source (Yang et al., 2021a; Tan et al., 2019a). Therefore, studying the
72 radical chemistry in the MBL provides a valuable opportunity to test the current
73 understanding of atmospheric oxidation mechanisms in a natural setting.

74 Since the earliest observations off the coast of northern Norfolk in the Weybourne
75 Atmospheric Observatory Summer Experiment in June 1995 (WAOSE95), more
76 observations and simulations of radical chemistry in the MBL environment have been
77 conducted using ground-based, airborne, and shipborne instruments (Qi et al., 2007;
78 Kanaya et al., 2002; Kanaya et al., 2001; Mallik et al., 2018; Woodward-Massey et al.,
79 2022a; Carpenter et al., 2011; Grenfell et al., 1999; Brauers et al., 2001; Whalley et al.,
80 2010). Most field measurements have yielded well-reproduced OH and HO₂
81 concentration profiles via chemical mechanisms, with differences of within ~20%.

82 However, the base model is not sufficient to describe the radical chemistry in some
83 exceptional cases, especially in regard to the HO₂ radical. Considering the practical
84 association between halogen (Cl, Br, and I) chemistry and heterogeneous chemistry in
85 marine new particle formation, particularly the involvement of heterogeneous iodine-
86 organic chemistry, exploring the synchronous influence of these mechanisms on HO_x
87 (OH and HO₂) radical chemistry in the MBL region is a worthy endeavor (Xu et al.,
88 2022; Huang et al., 2022). The mixing of air masses of continental and marine origins
89 can lead to more variability in radical concentrations. During seasonal measurements
90 of both OH and HO₂ in the Atlantic Ocean, variance analysis indicated that around 70%
91 of the variance of OH and HO₂ was due to diurnal behavior (in the form of photolysis
92 frequency), while the remaining variance was attributed to long-term seasonal cycles
93 (in the form of the changes in O₃, CO and air mass contribution) (Vaughan et al.,
94 2012).

95 The Chinese economy has undergone rapid development in recent years, and the
96 co-occurrence of primary and secondary regional pollution has become a severe
97 problem (Lu et al., 2019; Liu et al., 2022c). The interactions between air pollutants
98 from upwind cities, shipping vessels, and other anthropogenic emissions lead to
99 precursor accumulation (Sun et al., 2020; Zeren et al., 2022). The background ozone
100 concentration in key regions of China has increased year by year, highlighting the
101 significant influence of anthropogenic activities on the atmospheric oxidation in
102 background regions in China (Wang et al., 2009; Chen et al., 2022). However, little
103 research has been dedicated to the radical chemistry and oxidation mechanism in
104 regions with both coastal and continental features. To fill this research gap, in this
105 study, a field campaign was conducted on photochemistry in the MBL at a coastal site
106 in the Pearl River Delta. The OH and HO₂ radicals associated with other related
107 species were measured in October 2019, and the radical-related oxidation process was
108 identified to determine the photochemical efficiency in the marine atmosphere.

109 **2 Materials and methods**

2.1 Site description

As shown in Fig. 1(a), this observation campaign lasted for 11 days from October 18 to October 28, 2019, in Yangmeikeng (YMK, 22.55°N, 114.60°E), a coastal site in Shenzhen, Pearl River Delta. As the core city of the Greater Bay Area, Shenzhen is bordered by Dongguan to the north, Huizhou to the east, and Hong Kong to the south. The YMK site is on the Dapeng Peninsula, to the southeast of Shenzhen, between Mirs Bay and Daya Bay. As it is adjacent to the port of Hong Kong, precursors from ship emissions may influence the atmospheric chemistry. The site is a part of Shenzhen Ecological Monitoring Center station, approximately 35 m above sea level, and the sea is approximately 150 m to the east. No apparent local emissions exist, and the surrounding forest is lush (Fig. 1(b)). Previous literatures reported the monoterpane concentration in the YMK site, with a daily mean of 0.187 ppb (Zhu et al., 2021). Abundant biogenic emissions will likely influence the local chemistry. In addition to anthropogenic and vegetation emissions, the site is also affected by the synchronization of plumes from northern cities and the South China Sea (Niu et al., 2022; Xia et al., 2021). Due to its significant time-varying pollution characteristics, this area is an ideal site for studying the effects of plume transport on atmospheric oxidation.

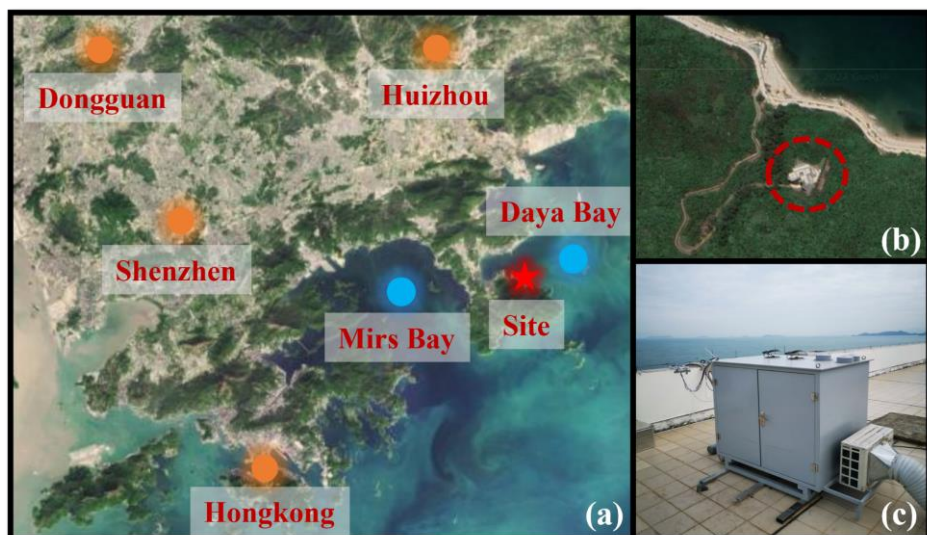


Fig. 1. Details of the observation site. (a) The location of the measurement site and surrounding cities (source: © Google Earth). (b) The close shot of the measurement site location. (c) The actual image for the LIF-Box.

Using the hybrid single-particle Lagrangian integrated trajectory (HYSPLIT)

model, the 24-h backward trajectories on special days were obtained. In Fig. S1, the red, blue, and green trajectories represent the results at altitudes of 100, 500, and 1000 m above ground level, respectively. Two typical transportation pathways dominated the air parcels. One originated from the northern megacities in the Pearl River Delta (defined as the land mass, LAM), especially on October 18, 19, and 27. In contrast, a clean air mass from the east or northeast was mainly transported to the observation site from the ocean (defined as the ocean mass, OCM), with representative episodes on October 22, 25, and 26.

2.2 Instrumentation

2.2.1 HO_x radical measurements

The OH and HO₂ radicals were measured via laser-induced fluorescence (LIF). The OH radical can be directly measured by exciting the fluorescence using a 308-nm laser. HO₂ is converted into the OH radical via chemical transformation and then detected in the form of OH radical. The self-developed instrument, the Anhui Institute of Optics Fine Mechanics-LIF (AIOFM-LIF), was used to conduct the measurements (Zhang et al., 2022a; Wang et al., 2021; Wang et al., 2019). This system has been used in key regions of China, including the Yangtze River Delta, Pearl River Delta, and Chengdu-Chongqing region, and achieved good performance in a comparison experiment with a LIF system jointly developed by Forschungszentrum Jülich and Peking University (PKU-LIF) (Zhang et al., 2022b).

The system and detection interference process have been described in detail in previous studies (Zhang et al., 2022a). Briefly, the system consists of a laser output module, a radical detection module, and a control and data acquisition module. These modules are integrated into a sampling box with constant temperature and humidity control (Fig. 1(c)). The laser output module is a union of an Nd:yttrium-aluminum-garnet (YAG) solid-state laser, a 532-nm laser output, and a tunable dye laser. The radical detection module utilized a single pass laser configuration, and the laser beam had a diameter of 8 mm. OH and HO₂ fluorescence cells are combined in parallel and share a common axial optical path. The 308-nm laser is introduced into the HO₂ cell

161 first and then into the OH cell via an 8-m fiber. To maintain the detection efficiency,
162 the power in the OH fluorescence cell should be at least 15 mW. In the detection
163 process, a set of lenses was deployed and positioned in front of the microchannel plate
164 detector (MCP) to boost the fluorescence collection capacity. Each MCP detector
165 contains a timing control instrument to optimize the signal-to-noise ratio (SNR) of the
166 fluorescence detection. Efficient ambient air sampling was achieved using an
167 aluminum nozzle (0.4 mm orifice), and the pressure in the chamber was maintained at
168 400 Pa via a vortex vacuum pump (XDS35i, Edwards) to reduce fluorescence
169 quenching.

170 A wavelength modulation for the background measurement that periodically
171 switches from an on-resonant state to a non-resonant state has been widely used to
172 obtain spectral zero. Since the ozone photolysis interference is due to the laser light
173 itself, wavelength modulation does not allow removing it. Through laboratory
174 experiments, at 20 mW laser energy, every 1% water vapor concentration and 50 ppb
175 ozone concentration can generate a 2.5×10^5 cm⁻³ OH concentration. The results in
176 this paper have subtracted the ozone photolysis interference (Fig. S2). In terms of
177 system design, the AIOFM-LIF system incorporates a short-length inlet design to
178 minimize interferences from ozonolysis and other unknown factors (the distance from
179 radical sampling to fluorescence excitation is ~150 mm). An OH measurement
180 comparison with an interference-free instrument, PKU-LIF, was conducted in a real
181 atmosphere in a previous study (Zhang et al., 2022b). The ozonolysis interference on
182 the measurement consistency of both systems was excluded under high-VOCs
183 condition. Overall, the key parameters related to ozonolysis reactions (O₃、 alkenes、
184 isoprene and NOx) in YMK was similar to that during the intercomparison
185 experiment, implies that the chemical conditions do not favor the generation of
186 potential interference to OH measurement (Table S1). For HO₂ measurement, the NO
187 gas (2% in N₂) was utilized to achieve HO₂-to-OH conversion. NO was passed
188 through a ferrous sulfate filter to remove impurities (NO₂, HONO, and so on) before
189 being injected into the detection cell. The NO concentration ($\sim 1.6 \times 10^{12}$ cm⁻³)

190 corresponding to a conversion efficiency of ~15% was selected to avoid $\text{RO}_2 \rightarrow \text{HO}_2$
191 interference (especially from RO_2 radicals derived from long-chain alkanes ($\text{C} \geq 3$),
192 alkenes, and aromatic hydrocarbons). Previous study denoted that the percentage
193 interference from alkene-derived RO_2 under these operating conditions was no more
194 than 5% (Wang et al., 2021).

195 A standard HOx radical source was used to complete the calibration of the
196 detection sensitivity (Wang et al., 2020). The radical source is based on the
197 simultaneous photolysis of $\text{H}_2\text{O}/\text{O}_2$ by a 185 nm mercury lamp. Humidified air flow is
198 introduced to produce equal amounts of OH and HO_2 radicals after passing the
199 photolysis region. The flow remained in a laminar condition with a maximum flow
200 rate of 20 SLM (standard liters per minute). As the luminous flux in photolysis region
201 is difficult to accurately measure, the linearly correlation between ozone concentration
202 and 185 nm light flux was established. Ozone concentration in the flow tube was
203 measured by a home-made Cavity Ring Down Spectrometer (CRDS, and the
204 detection limit is 15 ppt@30 s, 1σ). Mercury lamp intensity is fine-tuned to establish a
205 correlation between light intensity and ozone concentration. The instrument was
206 calibrated every 1 or 2 days (except for shutdown during rainy periods), and the
207 sensitivity used for the data processing was an average of all of the calibration results.
208 In the YMK campaign, the relative humidity varied between 40 – 80% (Fig. S3). In
209 order to test different atmospheric conditions, both low (~40%) and high (~70%)
210 levels of water vapor were selected to produce OH and HO_2 radicals for calibration,
211 and the corresponding HOx concentration obtained from the standard source was 1.0
212 $\times 10^9 \text{ cm}^{-3}$ and $1.8 \times 10^9 \text{ cm}^{-3}$, respectively (Zhang et al., 2022b).

213 Considering the system uncertainty and calibration uncertainty, the detection
214 limits of the OH and HO_2 radicals were $3.3 \times 10^5 \text{ cm}^{-3}$ and $1.1 \times 10^6 \text{ cm}^{-3}$ (60 s, 1σ),
215 respectively. At a typical laser power of 15 mW, the measurement accuracy for OH
216 and HO_2 measurement was 13% and 17% (1σ), respectively.

217 **2.2.2 Supporting measurements**

218 In addition to measuring the HOx radicals, an extensive suite of relevant species

219 was also measured close to the LIF instrument to improve the analysis of the radical
220 photochemistry. Detailed information about the measurement instrument is presented
221 in Table S2, including the meteorological parameters (wind speed (WS), wind
222 direction (WD), temperature (T), relative humidity (RH), pressure (P), and solar
223 radiation (J-values)) and chemical parameters (ozone (O₃), carbon monoxide (CO),
224 sulfur dioxide (SO₂), HONO, NO, NO₂, HCHO, NMHCs, and particulate matter
225 (PM_{2.5})). HONO measurement was conducted using a commercial Long-Path
226 Absorption Photometer (LOPAP). The LOPAP method utilizes two absorption tubes
227 in series for differential correction, which effectively eliminates the influence of
228 known interfering substances such as NO₂ and N₂O₅, offering an advantage over
229 traditional wet chemistry methods. Zero air measurements were taken every 8 hours
230 for a duration of 20 minutes to correct for instrument baseline fluctuations. This
231 method has been extensively tested for its suitability in detecting HONO in complex
232 atmospheric conditions, as demonstrated in previous studies by (Yang et al., 2022a;
233 Yang et al., 2021b; Wang et al., 2023). Eight measured photolysis rates ($j(\text{NO}_2)$,
234 $j(\text{H}_2\text{O}_2)$, $j(\text{HCHO})$, $j(\text{HONO})$, $j(\text{NO}_2)$, $j(\text{NO}_3)$, $j(\text{O}_1\text{D})$) were used as model constraints.
235 In addition to HCHO, other volatile organic compounds (VOCs) were detected using
236 a gas chromatograph coupled with a flame ionization detector and mass spectrometer
237 (GC-FID-MS). Ninety-nine types of VOCs, including C₂–C₁₁ alkanes, C₂–C₆ alkenes,
238 C₆–C₁₀ aromatics, halohydrocarbons, and some oxygenated VOCs (OVOCs), were
239 observed using the GC-FID-MS at a 1-h time interval. Only isoprene was considered
240 as a representative of biogenic VOCs (BVOCs). All of the instruments were located
241 close to the roof of the monitoring building, nearly 12 m above the ground to ensure
242 that all of the pollutants were located in a homogeneous air mass.

243 **2.3 Model description**

244 A 0-D chemical box model incorporating a condensed mechanism, the regional
245 atmospheric chemistry mechanism version 2-Leuven isoprene mechanism (RACM2-
246 LIM1), was used to simulate the radical concentrations and the generation of ozone
247 (Stockwell et al., 1997; Griffith et al., 2013; Tan et al., 2017). The meteorological

parameters, pollutants, and precursor concentrations mentioned in Section 2.2.2 were input into the model as boundary conditions. All of the constraints were unified to a temporal resolution of 15 min through averaging or linear interpolation. The overall average during the observations was substituted for large areas of missing data due to instrument maintenance or failure. Three days of data were entered in advance as the spin-up period, and a synchronized time-dependent dataset was eventually generated. The hydrogen (H_2) and methane (CH_4) concentrations were set to fixed values of 550 ppb and 1900 ppb, respectively. The physical losses of species due to processes such as deposition, convection, and advection were approximately replaced by an 18 h atmospheric lifetime, corresponding to first order loss rate of ~ 1.5 cm/s (by assuming a boundary layer height of about 1 km). The sensitivity analysis shows that when the lifetime changes within 8 – 24 hours, the values differed less than 5% for both OH , HO_2 , k_{OH} (Fig. S4). According to the measurement accuracy, the simulation accuracy of the model for the OH and HO_2 radicals was 50% (Zhang et al., 2022a).

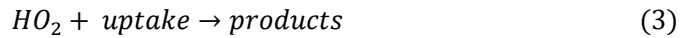
In addition, another steady-state calculation method (PSS) can also be used to estimate the concentrations of OH and HO_2 radicals (Eq. (1)(2), (Woodward-Massey et al., 2022b; Slater et al., 2020)). Since the k_{OH} and RO_2 concentrations were not obtained in this observation, simulated values are used as substitutes. Other radical and reactive intermediates are actual values that measured from the instruments in Table S2.

$$[OH]_{PSS} = \frac{j_{HONO}[HONO] + \varphi_{OH}j(O^1D)[O_3] + k_{HO_2+NO}[NO][HO_2]}{k_{OH}} \quad (1)$$

$$[HO_2]_{PSS} = \frac{k_{CO+OH}[CO][OH] + j_{HCHO}[HCHO] + k_{RO_2+NO}[NO][RO_2]}{k_{HO_2+NO}[NO]} \quad (2)$$

Considering the environmental characteristics of the MBL, the gas-phase mechanisms for bromine (Br) and iodine (I) were introduced into the base model to diagnose the impacts of the reactive bromine and iodine chemistry. The details of the mechanisms involved are listed in Tables S3 and S4. The halogen species were not available in the YMk site, so the typical levels of BrO and IO concentration in MBL site was used as a reference value (average daytime concentration of ~ 5 ppt) (Xia et al., 2022; Bloss et al., 2010; Whalley et al., 2010).

277 The heterogeneous uptake of HO₂ is considered to play an important role in the
278 MBL region (Whalley et al., 2010; Zou et al., 2022; Woodward-Massey et al., 2022b).
279 In order to assess the impact of HO₂ uptake on HOx radical chemistry, we
280 incorporated HO₂ uptake reaction into the base model (Eq. (3) - (5)).



282
$$k_{HO_2+\text{uptake}} = \frac{\gamma \times ASA \times \nu_{HO_2}}{4} \quad (4)$$

283
$$\nu_{HO_2} = \sqrt{\frac{8 \times R \times T}{0.033 \times \pi}} \quad (5)$$

284 Here, ASA represents the aerosol surface area [$\mu\text{m}^2 \text{ cm}^{-3}$], which can be estimated
285 as 20 times the PM_{2.5} concentration [$\mu\text{g}/\text{cm}^3$]. ν_{HO_2} [cm^{-1}] can be calculated using Eq.
286 (5), where T and R represent the temperature and gas constant, respectively. The
287 heterogeneous uptake coefficient (γ) for HO₂ usually has high uncertainty, with typical
288 values ranging from 0 to 1 (Song et al., 2021). In this study, we set γ to 0.08 to
289 evaluate the influence of HO₂ uptake on radical concentrations.

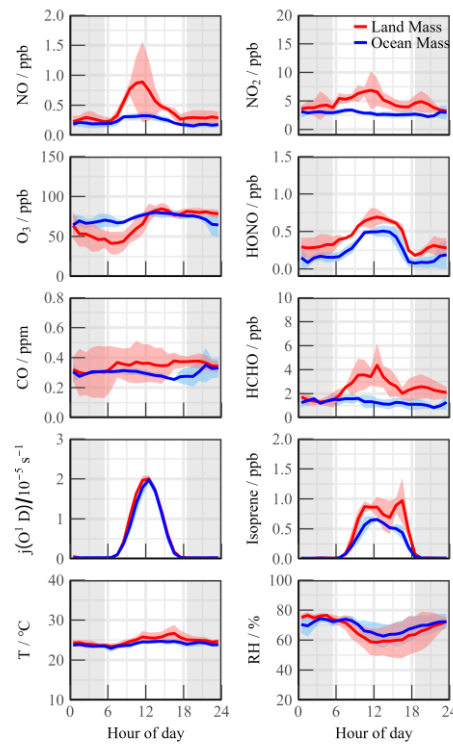
290 3 Results

291 3.1 Meteorological and chemical parameters

292 Fig. S3 presents the time series of the main meteorological parameters and
293 pollutants during the observation period at the YMK site. Except for on 2 days,
294 October 26 and 28, the meteorological characteristics of the other days were generally
295 stable. The daily maximum T, RH, and J-values did not vary significantly. The
296 suitable temperature (20–30°C) and humidity (40–80%) conditions promoted the
297 stable oxidation of the diurnal photochemistry. The peak $j(O^1D)$ value was
298 approximately $2.0 \times 10^{-5} \text{ s}^{-1}$, exhibiting the typical characteristics of intense light
299 radiation in autumn in the Pearl River Delta region (Yang et al., 2022a; Tan et al.,
300 2022).

301 As typical marine air components, the concentrations of NOx, CO, PM_{2.5}, and
302 other pollutants were lower than those detected in other observation campaigns in
303 both urban and suburban areas in the Pearl River Delta region (Tan et al., 2019b; Lu et

304 al., 2012; Yang et al., 2022b). Several observation campaigns have discovered the
 305 relationship between wind direction and radical chemistry (Lu et al., 2012; Fuchs et
 306 al., 2017; Niu et al., 2022). Although there was no apparent wind speed condition, the
 307 dominant air mass still influenced the pollutant concentrations due to the particularity
 308 of the marine site.



309
 310 **Fig. 2.** Mean diurnal profiles of measured trace gases parameters during Land mass and Ocean mass episodes. The
 311 coloured shadows denote the 25 and 75% percentiles. The grey areas denote nighttime.

312 During the OCM period, the NOx and HCHO concentrations exhibited relatively
 313 clean characteristics that were consistent with those previously observations in open
 314 ocean (RHAMBLe, SOS, CHABLIS and ALBATROSS, Table 1). Isoprene, a
 315 representative BVOC, achieved a diurnal concentration of 0.58 ± 0.06 ppb, indicated
 316 slightly local emissions could have impacted the concentrations of the precursor
 317 species even in OCM sector. The ozone concentration in the YMk site was always at
 318 the critical value of the updated Class I standard (GB3095-2012, average hourly O₃ of
 319 81 ppb at 25°C and 1013 kPa). The occurrence of fewer emissions reduced the
 320 titration effect, resulting in the ozone exhibiting no apparent diurnal trend on some of
 321 the dates and a high background value at night (78.1 ± 7.6 ppb).

322 As a coastal site, chemical conditions could be influenced by local land emissions

323 depending on the wind direction. Compared with the OCM period, the meteorological
 324 conditions (T, RH, and J-values) changed slightly during the LAM episode, but the
 325 pollutants were accumulated due to the transport of the plume from the northern cities
 326 (Fig. 2). The CO and PM_{2.5} concentrations exhibited good consistency and even mild
 327 pollution features ((0.36 ± 0.12 ppm) and (37.70 ± 7.91 µg/m³), respectively),
 328 reflecting the influence of human activities. Both NO and NO₂ peaked at around
 329 10:00, exhibiting prominent pollution characteristics. HONO exhibited a distribution
 330 with high daytime (0.66 ± 0.08 ppb) and low nighttime (0.33 ± 0.09 ppb)
 331 concentrations. This unique distribution of HONO has been observed in remote
 332 environments in several previous observation campaigns (Jiang et al., 2022; Crilley et
 333 al., 2021). High HONO concentration in the daytime will affect the chemical
 334 composition of the atmosphere and the secondary pollution generation.

335 **Table 1.** Summary of radical concentrations and related species concentrations at MBL. All data are listed as the
 336 average in noontime (10:00~15:00).

Campaign	Location	Category	Date	OH (10 ⁶ cm ⁻³)	HO ₂ (10 ⁸ cm ⁻³)	HCHO (ppb)	HONO (ppb)	NOx (ppb)	O ₃ (ppb)	Reference
WAOSE95	Weybourne, UK	Coastal	1995 (Jun)	5.0	-	1.50	0.10	<2.0	40.0	(Grenfell et al., 1999)
ALBATROSS	Atlantic Ocean	Open ocean	1996 (Oct-Nov)	7.0	-	0.50	-	-	25.0	(Brauers et al., 2001)
EASE96	Mace Head, Ireland	Coastal	1996 (Jul-Aug)	2.3	2.6	-	-	~1.0	45.0	(Carslaw et al., 1999)
EASE97	Mace Head, Ireland	Coastal	1997 (Apr-May)	1.8	1.0	0.70	-	0.95	46.0	(Creasey et al., 2002)
ORION99	Okinawa Island, Japan	Coastal	1999 (Aug)	4.0	4.3	-	0.20	6.3	23.0	(Kanaya et al., 2001)
RISOTTO	Rishiri Island, Japan	Coastal	2000 (June)	7.4	3.1	-	-	0.45	-	(Kanaya et al., 2002)
RISFEX	Rishiri Island, Japan	Coastal	2003 (Aug)	2.7	1.5	-	-	0.2	28.0	(Qi et al., 2007)
CHABLIS	Antarctica	Open ocean	2005 (Jan-Feb)	1.0	1.1	0.12	0.007	0.02	7.0	(Bloss et al., 2010)
RHaMBLe	Atlantic Ocean	Open ocean	2007 (May-Jun)	9.0	6.0	0.30	-	0.014	35.0	(Whalley et al., 2010)
SOS	Cape Verde, Atlantic Ocean	Open ocean	2009 (Jun; Sep)	9.0	4.0	1.9	-	0.050	40.0	(Carpenter et al., 2011)
CYPHEX	Cyprus, Mediterranean	Coastal	2014 (Jul)	5.8	6.3	~1.0	~0.080	<1.0	69.0	(Mallik et al., 2018)
ICOZA (NW-SE)	North Norfolk, UK	Coastal	2015 (Jul)	3.0	1.4	0.9	0.052	2.0	39.0	(Woodward- Massey et al., 2022b)
ICOZA (SW)	North Norfolk, UK	Coastal	2015 (Jul)	4.1	1.0	1.1	0.097	3.0	31.0	(Woodward- Massey et al., 2022b)
HT	Hok Tsui, China	Coastal	2020 (Oct-Nov)	4.9	-	1.0	0.15	~4.0	65.0	(Zou et al., 2022)

YMK (Land Mass)	Shenzhen, China	Coastal	2019 (Oct)	7.1	5.2	3.4	0.66	6.4	75.6	This work
YMK (Ocean Mass)	Shenzhen, China	Coastal	2019 (Oct)	4.5	4.9	1.2	0.48	3.0	78.1	This work

337

338 The detailed information for VOCs species during the YMK campaign has been
 339 added in the Table S5. The daily maximum NMHC concentration peaked at $27.81 \pm$
 340 9.91 ppb, and the maximum value of ~ 40 ppb occurred on October 27. Local
 341 biological emissions significantly affected the NMHC composition of the site, and
 342 isoprene achieved a noon maximum of 0.82 ± 0.16 ppb. Neither anthropogenic
 343 alkenes (2.21 ± 0.94 ppb) nor aromatic (1.31 ± 0.25 ppb) hydrocarbons were abundant,
 344 and OVOCs accounted for approximately 50% of the total. As a photochemical
 345 indicator, formaldehyde peaked at ~ 4 to ~ 8 ppb during the LAM episode, suggesting a
 346 more vigorous oxidation process. The HONO concentration was 6.8 times higher than
 347 the SW scenario in the ICOZA observation (a pollution period dominated by a
 348 southwest wind direction), while the HCHO concentration was 3.1 times higher.
 349 (Woodward-Massey et al., 2022b). The abundance of oxidation precursors (HONO,
 350 HCHO, O₃, and NMHCs) reflected the unique atmospheric conditions in the marine
 351 environment in China, which originated from the complex atmospheric pollution.

352 **3.2 HO_x radical concentrations and modelled OH reactivity**

353 Fig. 3(a)(b) shows the time series of the simulated and observed OH and HO₂
 354 radical concentrations during the observation campaign. The time series of the
 355 simulated OH reactivity (k_{OH}) is presented in Fig. 3(c). The observed OH and HO₂
 356 radicals exhibited significant diurnal trends. The daily maximum OH and HO₂ values
 357 were $(4.7\text{--}9.5) \times 10^6$ cm⁻³ and $(4.2\text{--}8.1) \times 10^8$ cm⁻³, respectively. The peak k_{OH} value
 358 was commonly less than 10 s⁻¹. Due to human activities, the simulated k_{OH} reached
 359 more than ~ 15 s⁻¹ on some days. The radical concentrations and reactivity exhibited
 360 similar trends, which differed from reports on urban and semi-urban areas where
 361 inorganic species (NO_x and CO) were the dominant controllers of k_{OH} (Zhang et al.,
 362 2022a; Tan et al., 2019b; Lou et al., 2010). The k_{OVOCs} was separated into $k_{OVOCs(Obs)}$
 363 and $k_{OVOCs(Model)}$ (Fig. 3(c)). Specifically, $k_{OVOCs(Obs)}$ includes the observed species

such as formaldehyde (HCHO), acetaldehyde (ACD), higher aldehydes (ALD), acetone (ACT), ketones (KET), and oxidation products of isoprene (MACR and MVK). The model-generated intermediates, such as glyoxal, methylglyoxal, methylethyl ketone, and methanol, are categorized as $k_{\text{OVOCs(Model)}}$. Approximately 50% of the total k_{OVOCs} are represented by unconstrained species ($k_{\text{OVOCs(Model)}}$), which contribute a daily k_{OH} of 1.39 s^{-1} . Overall, the observed OH and HO_2 concentrations were both well reproduced by the base model incorporating the RACM2-LIM1 mechanism. The observed OH was underestimated only on the first days, and a slight model overestimation happened on October 23&24. PSS calculation showed good agreement with the base model, providing evidence of the balance of radical internal consistency in the daytime. It should be noted that the OH reactivity of unmeasured VOCs may be underestimated due to the lumped groups in RACM2 mechanism.

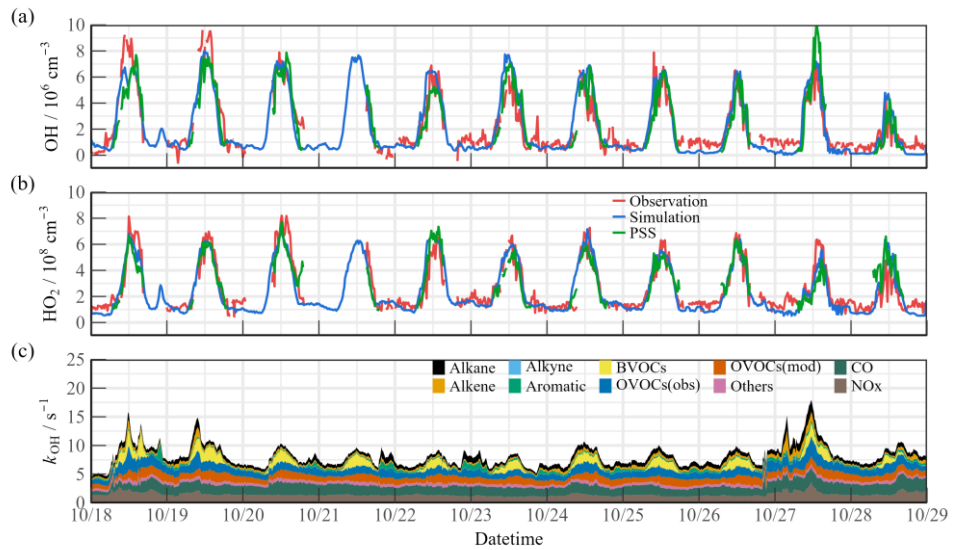
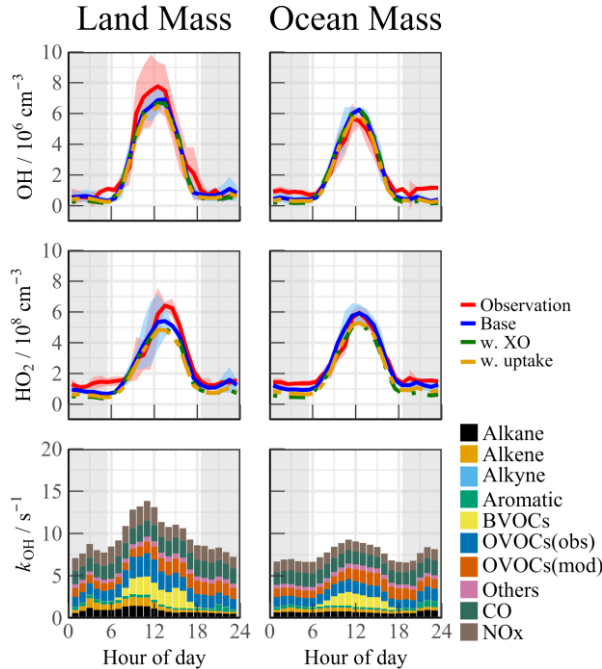


Fig. 3. Timeseries of the observed and modelled parameters for OH, HO_2 and k_{OH} during the observation period. (a) OH, (b) HO_2 , (c) k_{OH} .

The air mass transport of the precursors induced photochemistry accumulation, which was then reflected in the changes in the oxidation progress. It is worth comparing the concentrations and reactivities of the radicals by classifying the predominant air mass (Fig. 4). During the OCM period, the observed OH and HO_2 radicals could be reflected by the base chemical mechanism, with daily averages of $4.5 \times 10^6 \text{ cm}^{-3}$ and $4.9 \times 10^8 \text{ cm}^{-3}$, respectively. Compared to other campaigns (Table 1), the observed maximum values were within reasonable ranges (OH: $2 - 9 \times 10^6$

386 cm^{-3} ; HO_2 : $1 - 6 \times 10^8 \text{ cm}^{-3}$). Despite low NO_x levels during the OCM period, the
387 HO_2 radical was not overestimated using the base model, which was dissimilar to
388 many MBL observations (Bloss et al., 2010). However, both the OH and HO_2 radical
389 concentrations reached higher levels during the LAM-dominant period, indicating a
390 more active photochemical process (Section 4.1). The diel averages for the OH and
391 HO_2 radicals were $7.1 \times 10^6 \text{ cm}^{-3}$ and $5.2 \times 10^8 \text{ cm}^{-3}$, respectively, which were
392 notably higher than the levels reported in the ICOZA observations (Woodward-
393 Massey et al., 2022b). The base scenario underestimated both the OH and HO_2
394 concentrations between 10:00 and 15:00, and the observation-to-model ratio was
395 greater than 1.2. The calculated daily maximum total OH reactivity was 8.8 s^{-1} , and
396 nearly 70% of the reactivity was accounted for by the organic species, among which
397 the OVOCs were the largest contributor (30.6%). The anthropogenic alkanes, alkenes,
398 and aromatic hydrocarbons contributed less than 10% to the reactivity. Compared
399 with the OCM-dominant episode, the higher reactivity during the LAM period
400 indicated the occurrence of efficient recycling during the ROx (the sum of OH , HO_2 ,
401 and RO_2) propagation (12.4 s^{-1} vs. 8.8 s^{-1}). The higher contributions of the BVOCs
402 (only isoprene was considered, 15.6%) and OVOCs (30.2%) to the reactivity reflected
403 the diverse composition of the VOCs in the forest environment. Under enhanced
404 photochemistry, the calculated OH reactivity could be an underestimation of the total
405 OH reactivity, so a missing OH source may be masked. As a representative of the
406 OVOCs, HCHO reflects the photochemical level to a certain extent. As shown in Fig.
407 S5, a solid positive dependence between the OH_{obs} -to- OH_{mod} ratio and HCHO was
408 observed (the daytime data were restricted according to $j(\text{O}^1\text{D}) > 5 \times 10^{-6} \text{ s}^{-1}$). With
409 the increase of photochemical intensity, the ratio between the observed and simulated
410 OH radical showed an obvious mismatch. Obtaining the full magnitude of the radical-
411 related parameters is necessary to compensate for the discrepancy in the concentration
412 closure experiments.



413
 414 **Fig. 4.** Median diurnal profiles of the observed and modelled OH, HO₂, k_{OH} during LAM and OCM episodes.
 415 The coloured shadows for OH and HO₂ radicals denote the 25 and 75% percentiles. The grey areas denote
 416 nighttime.

417 Halogen species have been recognized as potent oxidizers that can boost
 418 photochemistry (Xia et al., 2022; Peng et al., 2021). A sensitivity test was performed
 419 by imposing BrO and IO into the base model to diagnose the impact of the halogen
 420 chemistry on the troposphere chemistry. The concentration of BrO and IO is set to ~5
 421 ppt, which is a typical level in MBL site (Xia et al., 2022; Bloss et al., 2010; Whalley
 422 et al., 2010). The details of the mechanisms involved are listed in Tables S3 and S4. In
 423 this scenario (Fig. 4, green line). The daytime concentration of HO₂ radical decreased
 424 by 8.5% and 13.3% during the LAM and OCM periods, respectively, compared to the
 425 base model. However, there was no significant change in the concentration of OH
 426 radicals (<3%). Traditionally, it is believed that the inclusion of halogen chemistry
 427 leads to higher modelled OH concentrations and lower modelled HO₂ concentrations.
 428 Therefore, the lack of an increase in OH concentration with the introduction of the
 429 halogen mechanism at the YMk site calls for further investigation (Fig. S6). By
 430 modifying the NO concentration in different levels (Scenario 1: [NO] × 150%,
 431 Scenario 2: base, Scenario 3: [NO] × 20%, Scenario 4: [NO] × 10%), the response of
 432 HO_x radicals to the halogen mechanism varied under different NO levels. As the

433 constrained NO increased from 30 ppt to 500 ppt, the reduction in HO₂ radicals due to
434 the Br and I mechanisms ranged between 10% and 20%. At elevated NO_x levels,
435 reactions between halogen radicals and NO_x occurred, inhibiting the formation of OH
436 radicals. In Scenario 1, the OH concentration even decreased by 3.5% when
437 introducing the halogen mechanism. When NO concentration was constrained around
438 30 ppt (Scenario 4), similar to those obtained in RHaMBLe/CYPHEX campaigns, the
439 modelled OH concentration increased by 14.4%, while the HO₂ concentration
440 decreased by approximately 20.8% (Whalley et al., 2010; Bloss et al., 2010).
441 Therefore, the sensitivity of OH radicals to the halogen mechanism in the YMK
442 region is primarily limited by the local NO_x concentration level.

443 Although the modelled and measured HO₂ showed good agreement, the effect of
444 HO₂ heterogeneous processes on the chemistry of HO_x radicals is also worth
445 exploring. The inclusion of heterogeneous processes ($\gamma = 0.08$) did reduce the
446 modelled HO₂ concentration for ~10% during both LAM and OCM periods (Fig. 4,
447 yellow line). This reduced agreement between observation and simulation emphasizes
448 the presence of a missing HO₂ source in the base model.

449 **4 Discussion**

450 **4.1 Experimental radical budget balance**

451 **4.1.1 OH radical**

452 A process-oriented experiment was conducted to investigate the photochemistry
453 progress from a budget balance perspective (Woodward-Massey et al., 2022a; Tan et
454 al., 2019b; Yang et al., 2021a). The OH was in a photostationary steady state due to its
455 short lifetime. The total OH removal rate was directly quantified from the union of the
456 OH concentration and the reactivity (Eq.(6)):

$$457 D(OH) = [OH] \times k_{OH}. \quad (6)$$

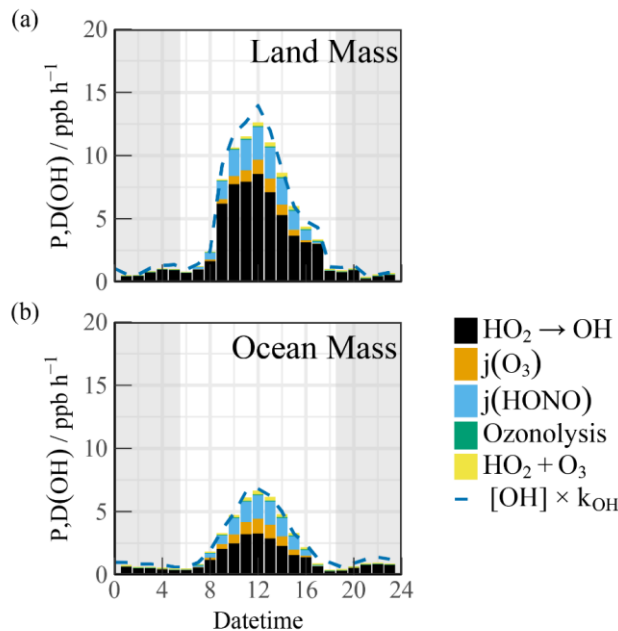
458 The total production rate of the OH radical was the sum of the primary sources
459 (O₃/HONO photolysis and ozonolysis reactions) and secondary sources (HO₂ + NO)
460 (Eq.(7)):

461
$$P(OH) = j_{HONO}[HONO] + \varphi_{OH}j(O^1D)[O_3] + \sum i \{ \varphi_{OH}^i k_{Alkenes+O_3}^i [Alkenes][O_3] \}$$

462
$$+ (k_{HO_2+NO}[NO] + k_{HO_2+O_3}[O_3])[HO_2]. \quad (7)$$

463 Here, φ_{OH} and φ_{OH}^i represent the OH yields in the O_3 photolysis and alkene
464 ozonolysis processes, respectively.

465 The diel profiles of the experimental OH budget during the LAM and OCM
466 periods are shown in Fig. 5. Both the observed OH and HO_2 radicals were introduced
467 into the budget calculations. Because k_{OH} was not measured during the observation
468 experiment, the simulated value was used to analyze the removal rate. Therefore,
469 $D(OH)$ should be considered a lower limit as it uses calculated rather than measured
470 k_{OH} (Yang et al., 2022b). During the OCM period, the $HO_2 + NO$ reaction accounted
471 for ~50% of the OH yield. The maximum of 6.6 ppb/h occurred at around 12:00. The
472 photolysis reactions could increase the daytime contributions of HONO and O_3 to
473 1.52 ppb/h and 0.84 ppb/h, respectively (10:00–15:00). The contribution of the non-
474 photolytic radical source (ozonolysis reactions) was almost negligible.



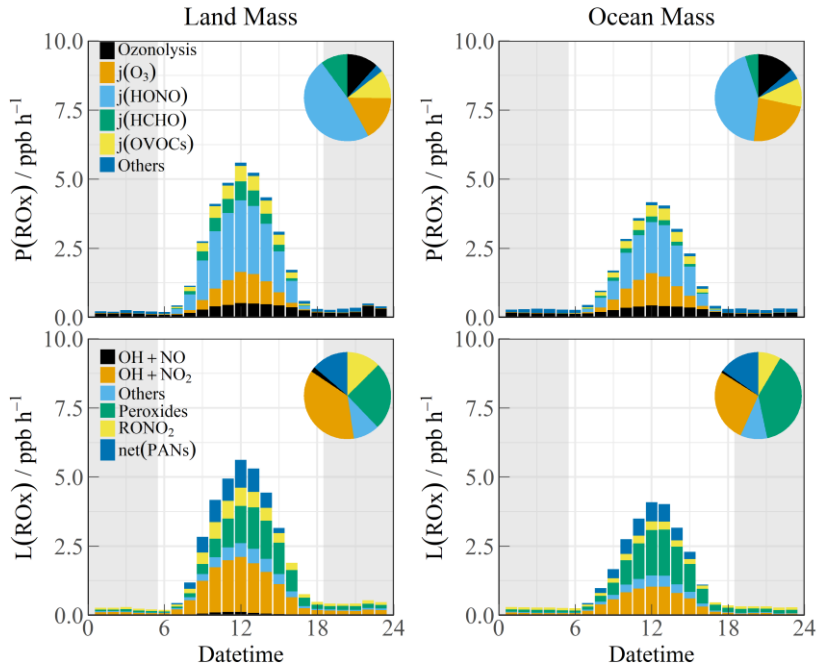
475 **Fig. 5.** The diurnal profiles of the experimental OH budget during (a) LAM and (b) OCM episodes. The blue
476 line denotes the OH destruction rate($[OH] \times k_{OH}$). The grey areas denote nighttime.
477

478 Compared with other marine observations, the calculated OH generation rate was
479 approximately twice that reported in the ICOZA and five times that obtained in the
480 RHAMBLe campaigns (Woodward-Massey et al., 2022a; Whalley et al., 2010).

481 During the LAM period, the OH generation rate reached a maximum of 12.6 ppb/h,
482 accompanied by a secondary source contribution of 67% (from the reaction between
483 HO₂ and NO) during the daytime, which was close to several observations related to
484 polluted plumes (Woodward-Massey et al., 2022a; Tan et al., 2019b; Lu et al., 2012;
485 Yang et al., 2022b). When the simulated k_{OH} was introduced into the experimental
486 budgets, the difference between P(OH) and D(OH) was less than 2 ppb/h.

487 **4.1.2 Total ROx radicals**

488 The budget analysis of the HO₂ and RO₂ radicals could not be performed well
489 due to the lack of RO₂ radical observation data. The diurnal profiles of the ROx
490 production (P(ROx)) and termination rate (L(ROx)) for the different air masses are
491 shown in Fig. 6. The P(ROx) could reach 3.36 ppb /h with an ocean plume. HONO
492 photolysis controlled nearly half of the primary sources (45.7%), and the daily
493 distribution was consistent with that of solar radiation. The ozone-related
494 contributions from photolysis and ozonolysis were approximately 46.6% (25.1% from
495 photolysis and 11.5% from ozonolysis, respectively). The remaining contribution was
496 from the photolysis of carbonyls (HCHO and OVOCs) (15.0%). The anthropogenic
497 contribution to the radical chemistry was not ignorable, and the ROx source in this
498 observation was exponentially higher than that in other MBL observations
499 (Woodward-Massey et al., 2022a; Stone et al., 2012; Whalley et al., 2010; Mallik et
500 al., 2018). The P(ROx) of the LAM was close to that in Shenzhen (~4 ppb/h) but was
501 significantly lower than that in Yufa (~7 ppb/h) and the BackGarden (~11 ppb/h) (Tan
502 et al., 2019b; Lu et al., 2012; Yang et al., 2022b). The reactions between ROx and
503 NOx and self-combination were the main pathways of radical termination (~70%).
504 The contribution of the formation of peroxy nitrate to the L(ROx) could not be ignored
505 in the daytime.



506
507 **Fig. 6.** The diurnal profiles of ROx budget during Land mass and Ocean mass episodes. The pie chart denotes
508 proportions in different parts during the daytime (10:00-15:00). The grey areas denote nighttime.

509 The high daytime HONO concentrations observed at the YMK site is a notable
510 phenomenon. Due to the high HONO concentration during the daytime, the photolysis
511 reaction made daytime contributions of 1.52 ppb/h and 2.19 ppb/h during the OCM
512 and LAM periods, respectively. As the only known gas-phase source, OH + NO
513 accounted for a negligible proportion of the HONO production rate. Given the
514 location of the site, HONO from cruise ship emissions is a possible component of the
515 primary anthropogenic source (Sun et al., 2020). Other active tropospheric HONO
516 sources (heterogeneous reactions with NO₂ and $p(NO_3^-)$ photolysis) are worthy of
517 consideration and significantly contribute to the atmospheric oxidation in the MBL
518 area (Zhu et al., 2022; Crilley et al., 2021).

519 **4.2 Local ozone production rate**

520 Peroxy radical chemistry is the essential photochemical source of tropospheric
521 ozone (F(Ox), Eq.(8)):

$$522 F(O_x) = k_{HO_2+NO}[NO][HO_2] + \sum_i(1 - \alpha_i)k_{RO_2^i+NO}[NO]RO_2^i \quad (8)$$

523 NO reacts with HO₂ and RO₂ radicals to form NO₂, and then, photolysis occurs to
524 form O₃ under solar radiation. NO₂ and ozone are the two sides of the oxidation
525 reservoir. The effect of local emissions on the photodynamic equilibrium can be
526 avoided by characterizing the photochemical production of the total oxidants (Tan et

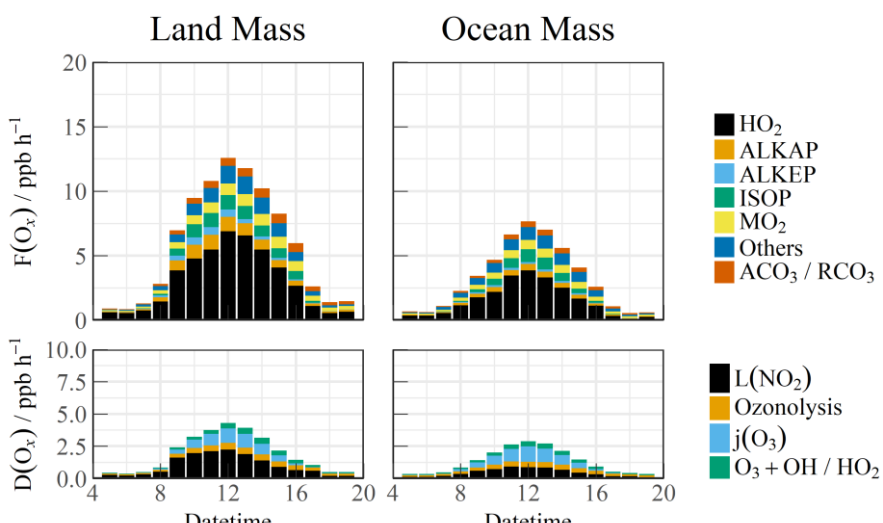
527 al., 2019b). α_i represents the organic nitrate yield, which affects the amount of NO_2
 528 that is produced from the reaction between RO_2 and NO (Tan et al., 2018b). Ox is
 529 mainly photochemically removed through ozone photolysis, ozonolysis, radical chain
 530 propagation ($\text{OH}/\text{HO}_2 + \text{O}_3$), and chain termination ($\text{OH} + \text{NO}_2$) reactions in the
 531 troposphere ($D(\text{Ox})$, Eq.(9)):

$$532 \quad D(\text{O}_x) = \varphi_{\text{OH}} j(\text{O}^1\text{D})[\text{O}_3] + \sum i \{ k_{\text{Alkenes}+\text{O}_3}^i [\text{Alkenes}][\text{O}_3] \} + (k_{\text{O}_3+\text{OH}}[\text{OH}] + \\ 533 \quad k_{\text{O}_3+\text{HO}_2}[\text{HO}_2])[\text{O}_3] + k_{\text{OH}+\text{NO}_2}[\text{OH}][\text{NO}_2] \quad (9)$$

534 The net formation rate $P(\text{O}_x)$ can be calculated by subtracting $D(\text{Ox})$ from $F(\text{Ox})$
 535 (Eq.(10)):

$$536 \quad P(\text{O}_x) = F(\text{O}_x) - D(\text{O}_x) \quad (10)$$

537 The simulated RO_2 radical concentration was introduced into the $F(\text{Ox})$
 538 calculation. The diurnal variations in the ozone generation in the different air masses
 539 are shown in Fig. 7. The contribution of the HO_2 radical to $F(\text{Ox})$ was approximately
 540 60%. The RO_2 radicals consisted of various types such as methyl peroxy (MO_2),
 541 acetyl peroxy radicals ($\text{ACO}_3/\text{RCO}_3$), and other radicals derived from alkanes
 542 (ALKAP), alkenes (ALKEP), and isoprene (ISOP), which accounted for an additional
 543 40% of the $F(\text{Ox})$. On a daytime basis, the maximum $F(\text{Ox})$ reached 7.4 ppb/h at
 544 around 12:00 in the OCM period, while a persistent-high value (maximum of 12.5
 545 ppb/h at 10:00–14:00) occurred in the LAM period. A vast amount of Ox was
 546 consumed in the nitric acid ($\text{OH} + \text{NO}_2$) formation pathways, i.e., higher than the
 547 ozonolysis removal. The daily averaged ozone production rates were 5.52 and 2.76
 548 ppb/h during the LAM and OCM periods, respectively.



549

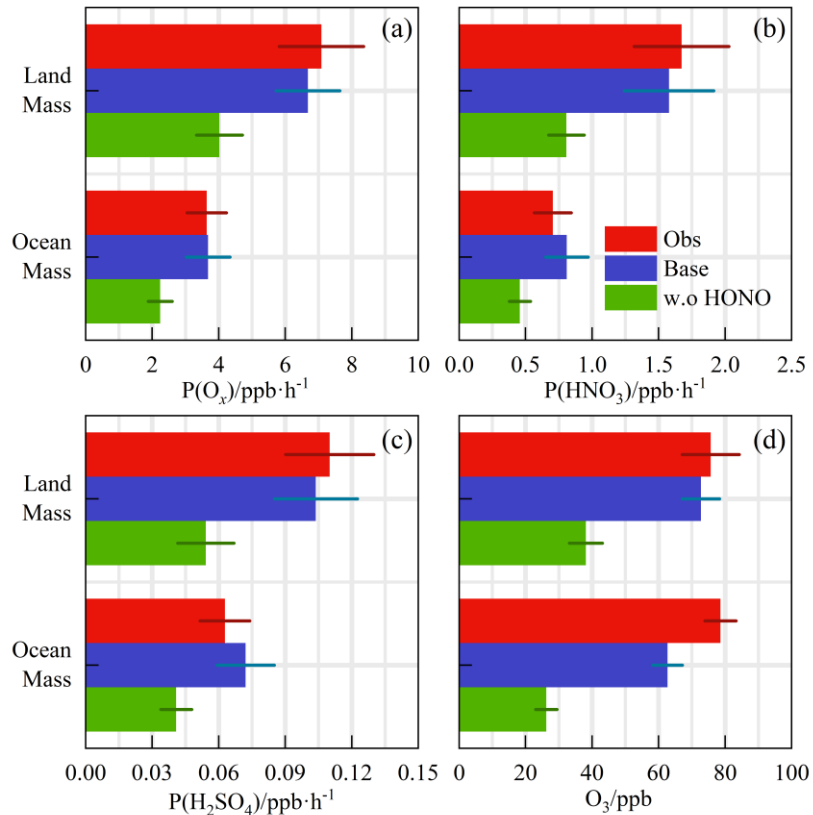
550

551 **Fig. 7.** The diurnal profiles of the speciation F(O_x) and D(O_x) during Land mass and Ocean mass episodes.
552 The data were calculated by the measured OH and HO₂ and modelled RO₂ radicals.553 **4.3 Relationship between precursors and oxidation rates**

554 Despite the low level of human activities, oxidation precursors have an extended
 555 lifetime in the stable atmosphere of coastal areas. Intensive photochemical reactions
 556 occur after the accumulation of precursors, resulting in local net ozone production
 557 comparable to that in the surrounding suburban environments (Zeren et al., 2022).
 558 Simultaneous observations of both urban and coastal settings in Shenzhen have
 559 indicated that the oxidation rates are comparable (Xia et al., 2021). The coupling of
 560 precursor transport and local photochemical processes in marine areas makes it
 561 meaningful to explore secondary pollution generation (Fig. 8(a), (b), and (c)). No
 562 obvious radical source was missing during the LAM and OCM periods, and the
 563 oxidation level was that expected from the base model. On a daytime basis, the mean
 564 diurnal profile of the P(O_x) reached ~7 ppb/h in the LAM period, and the average
 565 nitric acid (P(HNO₃)) and sulfuric acid (P(H₂SO₄)) production rates were ~1.6 and
 566 ~0.11 ppb/h, respectively. The P(HNO₃) production rate was similar to the average of
 567 observations in the Pearl River Delta region (~1.3 ppb/h), while that of the P(H₂SO₄)
 568 was only half the average level (~0.24 ppb/h) (Lu et al., 2013; Tan et al., 2019b; Yang
 569 et al., 2022b). During the OCM period, the characteristics of the ocean air mass
 570 alleviated the photochemical process, and the production rates of the secondary
 571 pollutants decreased by approximately half and were close to the average levels in
 572 winter (Ma et al., 2019).

573 Contrary to numerous ocean observations, in the YMK site, intensive oxidation
 574 was accompanied by a high diurnal HONO level (higher than 400 ppt) (Fig. 9). The
 575 ozone levels were consistent with the Grade I air quality standard and far exceeded
 576 the global background concentration (~40 ppb). Daytime photolysis reactions of
 577 HONO contributed 1.52 ppb/h and 2.19 ppb/h to P(RO_x) during the OCM and LAM
 578 periods, respectively, which were much higher than the values in several megacities
 579 during the photochemically polluted season (Tan et al., 2019a). Given the significance

580 of HONO photolysis in driving atmospheric chemistry, a sensitivity test was
 581 conducted without constraints on HONO (i.e., w/o HONO) to specifically quantify the
 582 contribution of HONO-induced secondary pollution. Only the homogeneous reaction
 583 ($\text{OH} + \text{NO}$) participated in the formation of HONO in the default mode without
 584 HONO input (Liu et al., 2022b).



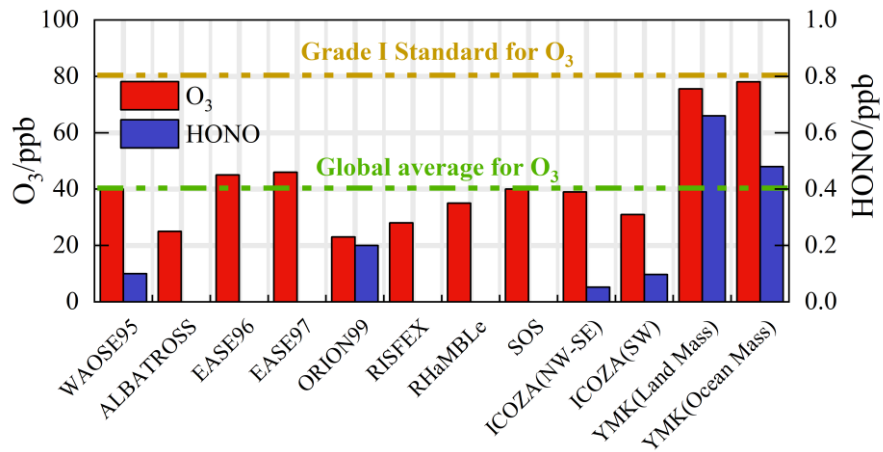
585

586 **Fig. 8.** The calculated reaction rates based on the observed concentrations for Land mass and Ocean mass
 587 episodes (a) $\text{P(O}_x\text{)}$, (b) $\text{P(HNO}_3\text{)}$, (c) $\text{P(H}_2\text{SO}_4\text{)}$. (d) The observed and modelled O_3 concentration with a first-order
 588 loss term. The deposition or mixing processes were equivalent to a lifetime of 18 hours to all species. All the rates
 589 and concentration are averaged for the daytime period between 10:00 and 15:00.

590

591 The modelled OH, HO_2 and RO_2 change when the model was unconstrained to
 592 HONO were shown in Fig. S7. After evaluation, in LAM and OCM sectors,
 593 concentration changes for OH were 46.9% and 43.2%, for HO_2 were 38.3% and
 594 34.3%, for RO_2 were 43.7% and 39.0%, respectively. The $\text{P(O}_x\text{)}$ was found to be 33%
 595 and 39% lower during the LAM and OCM periods, respectively. The nitric acid
 596 ($\text{P(HNO}_3\text{)}$) and sulfuric acid ($\text{P(H}_2\text{SO}_4\text{)}$) formation rates also increased
 597 simultaneously (~43% and ~48% for LAM and OCM sectors, respectively). The
 598 sensitivity test identified the privileged role of the HONO-related mechanisms in the
 OH chemistry, which resulted in a correlation between the efficient radical recycling

599 and secondary pollution.



600
601 **Fig. 9.** Summary of both ozone and HONO concentrations in previous marine observations. The
602 concentrations are averaged for the daytime period between 10:00 and 15:00.

603 A time-dependent box model was used to test the association between the HONO
604 chemistry and the local ozone generation (Fig. 8(d)). The loss of model-generated O₃
605 by deposition or mixing was represented as a first-order deposition rate corresponding
606 to a lifetime of 18 hours. Comparatively, removing the constraints on ozone and NO
607 while keeping NO₂ as a constraint is a commonly used method in the box model for
608 ozone prediction (Tan et al., 2018a). Considering the complexity of HONO chemistry,
609 we emphasize that this is a sensitivity test for ozone prediction, and its validity has
610 been examined through simulated comparisons under different HONO concentrations
611 (Fig. S8). The observed and modelled O₃ concentrations in Fig. 8(d) are averaged for
612 the daytime period between 10:00 and 15:00. The observed diurnal ozone
613 concentrations were 75.7 ppb and 78.6 ppb during the LAM and OCM periods,
614 respectively. The daytime ozone was well reproduced by the time-dependent box
615 model, and the deviation of the simulation was less than 20% (Fig. 8(d)). After
616 removing the HONO constraint, the simulated ozone concentrations were 38.2 and
617 26.3 ppb, i.e., 48% and 58% lower, during the LAM and OCM periods, respectively.
618 Simulated O₃ decreased from ~75 ppb to a global background, and daytime HONO
619 concentration were reduced to a low level (~70 ppt) (Woodward-Massey et al., 2022b;
620 Zhu et al., 2022; Xia et al., 2022). The elevated daytime HONO had an additional
621 effect on the oxidation in the background atmosphere. For coastal cities, the
622 particularity of the HONO chemistry in the MBL tends to influence the ozone-

623 sensitive system and eventually magnifies the ozone background. Therefore, the
624 promotion of oxidation by elevated precursor concentrations is worth considering
625 when formulating emission reduction policies. In regions where HONO
626 concentrations are elevated, the sources of HONO would need to be identified to aid
627 pollution mitigation policies.

628 **5 Conclusions**

629 Comprehensive observations of HO_x radicals and other relevant species were
630 conducted in October 2019 at a coastal site in the Pearl River Delta (the YMK site,
631 22.55°N, 114.60°E). The overall air pollutants exhibited typical coastal features due to
632 the scarce anthropogenic emissions. The daily maximum OH and HO₂ concentrations
633 were $(4.7\text{--}9.5) \times 10^6 \text{ cm}^{-3}$ and $(4.2\text{--}8.1) \times 10^8 \text{ cm}^{-3}$, respectively. The base RACM2-
634 LIM1 model satisfactorily reproduced both the observed OH and HO₂ radical
635 concentrations, but a slight overestimation of the OH radical occurred. The daily
636 maximum calculated total OH reactivity was 9.9 s^{-1} , and nearly 70% of the reactivity
637 was contributed by organic species.

638 In addition to anthropogenic and vegetation emissions, the synchronized air mass
639 transport from the northern cities and the South China Sea exerted a time-varying
640 influence on radical photochemistry and atmospheric oxidation. During the OCM
641 period, the observed OH and HO₂ radical concentrations could be reflected by the
642 base chemical mechanism, with daily average values of $4.5 \times 10^6 \text{ cm}^{-3}$ and 4.9×10^8
643 cm^{-3} , respectively.

644 In the episode that was dominated by ocean mass, the HO₂ + NO reaction
645 accounted for ~50% of the primary OH yield. A higher OH generation rate was
646 found(12.6 ppb/h) during the LAM period, and the secondary source accounted for 67%
647 of the total, which was similar to several observations in polluted plumes. Reactions
648 between RO_x and NO_x and self-combination were the main pathways of radical
649 termination (~70%), and the contribution of peroxy nitrate formation to the L(RO_x)
650 could not be ignored in the daytime.

651 Intensive photochemical reactions occur after the accumulation of precursors,
652 resulting in local net ozone production comparable to that in the surrounding suburban
653 environments. The daily average ozone production rates were 5.52 and 2.76 ppb/h in
654 the LAM and OCM periods, respectively. The rapid oxidation process was
655 accompanied by a higher diurnal HONO concentration (higher than 400 ppt). A non-
656 HONO-constrained sensitivity test was performed to quantify the HONO-induced
657 contribution to secondary pollution. After evaluation, the P(Ox) values were 33% and
658 39% lower during the LAM and OCM periods, respectively. The nitric acid (P(HNO₃))
659 and sulfuric acid (P(H₂SO₄)) formation rates also increased simultaneously (~43%
660 and ~48% for LAM and OCM sectors, respectively). Simulated O₃ decreased from
661 ~75 ppb to a global background, and daytime HONO concentration were reduced to a
662 low level (~70 ppt). For coastal cities, the particularity of the HONO chemistry in the
663 MBL tends to influence the ozone-sensitive system and eventually magnifies the
664 ozone background. Therefore, the promotion of oxidation by elevated precursor
665 concentrations is worth considering when formulating emission reduction policies.

666 **Financial support**

667 This work was supported by the National Natural Science Foundation of China
668 (62275250, U19A2044, 61905003), the Natural Science Foundation of Anhui
669 Province (No. 2008085J20), the National Key R&D Program of China
670 (2022YFC3700301), the Anhui Provincial Key R&D Program (2022l07020022), and
671 the Beijing Municipal Natural Science Fund for Distinguished Young Scholars (grant
672 no. JQ21030).

673 **Data availability**

674 The data used in this study are available from the corresponding author upon request
675 (rzhu@aiofm.ac.cn).

676 **Author contributions**

677 WQ Liu, PH Xie, RZ Hu contributed to the conception of this study. GX Zhang and
678 RZ Hu performed the data analyses and manuscript writing. All authors contributed to
679 measurements, discussed results, and commented on the paper.

680 **Competing interests**

681 The contact author has declared that none of the authors has any competing interests.
682
683

684 **References**

685 Bloss, W. J., Camredon, M., Lee, J. D., Heard, D. E., Plane, J. M. C., Saiz-Lopez, A., Bauguitte, S. J. B.,
686 Salmon, R. A., and Jones, A. E.: Coupling of HO_x, NO_x and halogen chemistry in the antarctic
687 boundary layer, *Atmos Chem Phys*, 10, 10187-10209, 10.5194/acp-10-10187-2010, 2010.

688 Brauers, T., Hausmann, M., Bister, A., Kraus, A., and Dorn, H.-P.: OH radicals in the boundary layer of
689 the Atlantic Ocean: 1. Measurements by long-path laser absorption spectroscopy, *Journal of*
690 *Geophysical Research*, 106, 7399, 10.1029/2000jd900679, 2001.

691 Carpenter, L. J., Fleming, Z. L., Read, K. A., Lee, J. D., Moller, S. J., Hopkins, J. R., Purvis, R. M.,
692 Lewis, A. C., Müller, K., Heinold, B., Herrmann, H., Fomba, K. W., van Pinxteren, D., Müller, C.,
693 Tegen, I., Wiedensohler, A., Müller, T., Niedermeier, N., Achterberg, E. P., Patey, M. D., Kozlova, E. A.,
694 Heimann, M., Heard, D. E., Plane, J. M. C., Mahajan, A., Oetjen, H., Ingham, T., Stone, D., Whalley, L.
695 K., Evans, M. J., Pilling, M. J., Leigh, R. J., Monks, P. S., Karunaharan, A., Vaughan, S., Arnold, S. R.,
696 Tschritter, J., Pöhler, D., Frieß, U., Holla, R., Mendes, L. M., Lopez, H., Faria, B., Manning, A. J., and
697 Wallace, D. W. R.: Seasonal characteristics of tropical marine boundary layer air measured at the Cape
698 Verde Atmospheric Observatory, *J Atmos Chem*, 67, 87-140, 10.1007/s10874-011-9206-1, 2011.

699 Carslaw, N., Creasey, D. J., Heard, D. E., Lewis, A. C., McQuaid, J. B., Pilling, M. J., Monks, P. S.,
700 Bandy, B. J., and Penkett, S. A.: Modeling OH, HO₂, and RO₂radicals in the marine boundary layer: 1.
701 Model construction and comparison with field measurements, *Journal of Geophysical Research: Atmospheres*, 104, 30241-30255, 10.1029/1999jd900783, 1999.

702 Chen, W., Guenther, A. B., Shao, M., Yuan, B., Jia, S., Mao, J., Yan, F., Krishnan, P., and Wang, X.:
703 Assessment of background ozone concentrations in China and implications for using region-specific
704 volatile organic compounds emission abatement to mitigate air pollution, *Environ Pollut*, 305, 119254,
705 10.1016/j.envpol.2022.119254, 2022.

706 Creasey, D. J., Heard, D. E., and Lee, J. D.: Eastern Atlantic Spring Experiment 1997 (EASE97) 1.
707 Measurements of OH and HO₂concentrations at Mace Head, Ireland, *Journal of Geophysical Research: Atmospheres*, 107, ACH 3-1-ACH 3-15, 10.1029/2001jd000892, 2002.

708 Crilley, L. R., Kramer, L. J., Pope, F. D., Reed, C., Lee, J. D., Carpenter, L. J., Hollis, L. D. J., Ball, S.
709 M., and Bloss, W. J.: Is the ocean surface a source of nitrous acid (HONO) in the marine boundary
710 layer?, *Atmos Chem Phys*, 21, 18213-18225, 10.5194/acp-21-18213-2021, 2021.

711 Fuchs, H., Dorn, H. P., Bachner, M., Bohn, B., Brauers, T., Gomm, S., Hofzumahaus, A., Holland, F.,
712 Nehr, S., Rohrer, F., Tillmann, R., and Wahner, A.: Comparison of OH concentration measurements by
713 DOAS and LIF during SAPHIR chamber experiments at high OH reactivity and low NO concentration,
714 *Atmos Meas Tech*, 5, 1611-1626, 10.5194/amt-5-1611-2012, 2012.

715 Fuchs, H., Tan, Z., Lu, K., Bohn, B., Broch, S., Brown, S. S., Dong, H., Gomm, S., Haeseler, R., He, L.,
716 Hofzumahaus, A., Holland, F., Li, X., Liu, Y., Lu, S., Min, K.-E., Rohrer, F., Shao, M., Wang, B., Wang,
717 M., Wu, Y., Zeng, L., Zhang, Y., Wahner, A., and Zhang, Y.: OH reactivity at a rural site (Wangdu) in
718 the North China Plain: contributions from OH reactants and experimental OH budget, *Atmos Chem
719 Phys*, 17, 645-661, 10.5194/acp-17-645-2017, 2017.

720 Grenfell, J. L., Savage, N. H., Harrison, R. M., Penkett, S. A., Forberich, O., Comes, F. J., Clemitshaw,
721 K. C., Burgess, R. A., Cardenas, L. M., Davison, B., and McFadyen, G. G.: Tropospheric box-
722 modelling and analytical studies of the hydroxyl (OH) radical and related species: Comparison with
723 observations, *J Atmos Chem*, 33, 183-214, 10.1023/a:1006009901180, 1999.

724

725

726 Griffith, S. M., Hansen, R. F., Dusanter, S., Stevens, P. S., Alaghmand, M., Bertman, S. B., Carroll, M.
727 A., Erickson, M., Galloway, M., Grossberg, N., Hottle, J., Hou, J., Jobson, B. T., Kammrath, A.,
728 Keutsch, F. N., Lefer, B. L., Mielke, L. H., O'Brien, A., Shepson, P. B., Thurlow, M., Wallace, W.,
729 Zhang, N., and Zhou, X. L.: OH and HO₂ radical chemistry during PROPHET 2008 and CABINEX
730 2009-Part 1: Measurements and model comparison, *Atmos Chem Phys*, 13, 5403-5423, 10.5194/acp-
731 13-5403-2013, 2013.

732 Huang, R. J., Hoffmann, T., Ovadnevaite, J., Laaksonen, A., Kokkola, H., Xu, W., Xu, W., Ceburnis, D.,
733 Zhang, R., Seinfeld, J. H., and O'Dowd, C.: Heterogeneous iodine-organic chemistry fast-tracks marine
734 new particle formation, *Proc Natl Acad Sci U S A*, 119, e2201729119, 10.1073/pnas.2201729119, 2022.

735 Jiang, Y., Xue, L., Shen, H., Dong, C., Xiao, Z., and Wang, W.: Dominant Processes of HONO Derived
736 from Multiple Field Observations in Contrasting Environments, *Environmental Science & Technology*
737 Letters, 10.1021/acs.estlett.2c00004, 2022.

738 Kanaya, Y., Sadanaga, Y., Nakamura, K., and Akimoto, H.: Behavior of OH and HO₂ radicals during
739 the Observations at a Remote Island of Okinawa (ORION99) field campaign 1. Observation using a
740 laser-induced fluorescence instrument, *J Geophys Res-Atmos*, 106, 24197-24208,
741 10.1029/2000jd000178, 2001.

742 Kanaya, Y., Yokouchi, Y., Matsumoto, J., Nakamura, K., Kato, S., Tanimoto, H., Furutani, H., Toyota,
743 K., and Akimoto, H.: Implications of iodine chemistry for daytime HO₂levels at Rishiri Island,
744 *Geophys Res Lett*, 29, 45-41-45-44, 10.1029/2001gl014061, 2002.

745 Liu, C., Liu, G., Casazza, M., Yan, N., Xu, L., Hao, Y., Franzese, P. P., and Yang, Z.: Current Status and
746 Potential Assessment of China's Ocean Carbon Sinks, *Environ Sci Technol*, 56, 6584-6595,
747 10.1021/acs.est.1c08106, 2022a.

748 Liu, P., Xue, C., Ye, C., Liu, C., Zhang, C., Wang, J., Zhang, Y., Liu, J., and Mu, Y.: The Lack of
749 HONO Measurement May Affect the Accurate Diagnosis of Ozone Production Sensitivity, *ACS*
750 *Environmental Au*, 10.1021/acsenvironau.2c00048, 2022b.

751 Liu, T., Hong, Y., Li, M., Xu, L., Chen, J., Bian, Y., Yang, C., Dan, Y., Zhang, Y., Xue, L., Zhao, M.,
752 Huang, Z., and Wang, H.: Atmospheric oxidation capacity and ozone pollution mechanism in a coastal
753 city of southeastern China: analysis of a typical photochemical episode by an observation-based model,
754 *Atmos Chem Phys*, 22, 2173-2190, 10.5194/acp-22-2173-2022, 2022c.

755 Lou, S., Holland, F., Rohrer, F., Lu, K., Bohn, B., Brauers, T., Chang, C. C., Fuchs, H., Haeseler, R.,
756 Kita, K., Kondo, Y., Li, X., Shao, M., Zeng, L., Wahner, A., Zhang, Y., Wang, W., and Hofzumahaus, A.:
757 Atmospheric OH reactivities in the Pearl River Delta – China in summer 2006: measurement and
758 model results, *Atmos Chem Phys*, 10, 11243–11260, 10.5194/acp-10-11243-2010, 2010.

759 Lu, K. D., Guo, S., Tan, Z. F., Wang, H. C., Shang, D. J., Liu, Y. H., Li, X., Wu, Z. J., Hu, M., and
760 Zhang, Y. H.: Exploring atmospheric free-radical chemistry in China: the self-cleansing capacity and
761 the formation of secondary air pollution, *Natl. Sci. Rev.*, 6, 579-594, 10.1093/nsr/nwy073, 2019.

762 Lu, K. D., Hofzumahaus, A., Holland, F., Bohn, B., Brauers, T., Fuchs, H., Hu, M., Haeseler, R., Kita,
763 Kondo, Y., Li, X., Lou, S. R., Oebel, A., Shao, M., Zeng, L. M., Wahner, A., Zhu, T., Zhang, Y. H.,
764 and Rohrer, F.: Missing OH source in a suburban environment near Beijing: observed and modelled
765 OH and HO₂ concentrations in summer 2006, *Atmos Chem Phys*, 13, 1057-1080, 10.5194/acp-13-
766 1057-2013, 2013.

767 Lu, K. D., Rohrer, F., Holland, F., Fuchs, H., Bohn, B., Brauers, T., Chang, C. C., Haeseler, R., Hu, M.,
768 Kita, K., Kondo, Y., Li, X., Lou, S. R., Nehr, S., Shao, M., Zeng, L. M., Wahner, A., Zhang, Y. H., and
769 Hofzumahaus, A.: Observation and modelling of OH and HO₂ concentrations in the Pearl River Delta

770 2006: a missing OH source in a VOC rich atmosphere, *Atmos Chem Phys*, 12, 1541-1569,
771 10.5194/acp-12-1541-2012, 2012.

772 Ma, X. F., Tan, Z. F., Lu, K. D., Yang, X. P., Liu, Y. H., Li, S. L., Li, X., Chen, S. Y., Novelli, A., Cho,
773 C. M., Zeng, L. M., Wahner, A., and Zhang, Y. H.: Winter photochemistry in Beijing: Observation and
774 model simulation of OH and HO₂ radicals at an urban site, *Sci Total Environ*, 685, 85-95,
775 10.1016/j.scitotenv.2019.05.329, 2019.

776 Mallik, C., Tomsche, L., Bourtsoukidis, E., Crowley, J. N., Derstroff, B., Fischer, H., Hafermann, S.,
777 Hüser, I., Javed, U., Keßel, S., Lelieveld, J., Martinez, M., Meusel, H., Novelli, A., Phillips, G. J.,
778 Pozzer, A., Reiffs, A., Sander, R., Taraborrelli, D., Sauvage, C., Schuladen, J., Su, H., Williams, J., and
779 Harder, H.: Oxidation processes in the eastern Mediterranean atmosphere: evidence from the modelling
780 of HO_x; measurements over Cyprus, *Atmos Chem Phys*, 18, 10825-10847, 10.5194/acp-18-10825-
781 2018, 2018.

782 Niu, Y. B., Zhu, B., He, L. Y., Wang, Z., Lin, X. Y., Tang, M. X., and Huang, X. F.: Fast Nocturnal
783 Heterogeneous Chemistry in a Coastal Background Atmosphere and Its Implications for Daytime
784 Photochemistry, *Journal of Geophysical Research: Atmospheres*, 127, 10.1029/2022jd036716, 2022.

785 Peng, X., Wang, W. H., Xia, M., Chen, H., Ravishankara, A. R., Li, Q. Y., Saiz-Lopez, A., Liu, P. F.,
786 Zhang, F., Zhang, C. L., Xue, L. K., Wang, X. F., George, C., Wang, J. H., Mu, Y. J., Chen, J. M., and
787 Wang, T.: An unexpected large continental source of reactive bromine and chlorine with significant
788 impact on wintertime air quality, *Natl. Sci. Rev.*, 8, 10.1093/nsr/nwaa304, 2021.

789 Qi, B., Kanaya, Y., Takami, A., Hatakeyama, S., Kato, S., Sadanaga, Y., Tanimoto, H., and Kajii, Y.:
790 Diurnal peroxy radical chemistry at a remote coastal site over the sea of Japan, *Journal of Geophysical
791 Research*, 112, 10.1029/2006jd008236, 2007.

792 Slater, E. J., Whalley, L. K., Woodward-Massey, R., Ye, C., Lee, J. D., Squires, F., Hopkins, J. R.,
793 Dunmore, R. E., Shaw, M., Hamilton, J. F., Lewis, A. C., Crilley, L. R., Kramer, L., Bloss, W., Vu, T.,
794 Sun, Y., Xu, W., Yue, S., Ren, L., Acton, W. J. F., Hewitt, C. N., Wang, X., Fu, P., and Heard, D. E.:
795 Elevated levels of OH observed in haze events during wintertime in central Beijing, *Atmos Chem Phys*,
796 20, 14847-14871, 10.5194/acp-20-14847-2020, 2020.

797 Song, H., Lu, K., Dong, H., Tan, Z., Chen, S., Zeng, L., and Zhang, Y.: Reduced Aerosol Uptake of
798 Hydroperoxyl Radical May Increase the Sensitivity of Ozone Production to Volatile Organic
799 Compounds, *Environmental Science & Technology Letters*, 9, 22-29, 10.1021/acs.estlett.1c00893,
800 2021.

801 Stockwell, W. R., Kirchner, F., Kuhn, M., and Seefeld, S.: A new mechanism for regional atmospheric
802 chemistry modeling, *J Geophys Res-Atmos*, 102, 25847-25879, 10.1029/97jd00849, 1997.

803 Stone, D., Whalley, L. K., and Heard, D. E.: Tropospheric OH and HO₂ radicals: field measurements
804 and model comparisons, *Chemical Society reviews*, 41, 6348-6404, 10.1039/c2cs35140d, 2012.

805 Sun, L., Chen, T., Jiang, Y., Zhou, Y., Sheng, L., Lin, J., Li, J., Dong, C., Wang, C., Wang, X., Zhang,
806 Q., Wang, W., and Xue, L.: Ship emission of nitrous acid (HONO) and its impacts on the marine
807 atmospheric oxidation chemistry, *Sci Total Environ*, 735, 139355, 10.1016/j.scitotenv.2020.139355,
808 2020.

809 Tan, Z., Lu, K., Ma, X., Chen, S., He, L., Huang, X., Li, X., Lin, X., Tang, M., Yu, D., Wahner, A., and
810 Zhang, Y.: Multiple Impacts of Aerosols on O(3) Production Are Largely Compensated: A Case Study
811 Shenzhen, China, *Environ Sci Technol*, 10.1021/acs.est.2c06217, 2022.

812 Tan, Z., Lu, K., Jiang, M., Su, R., Wang, H., Lou, S., Fu, Q., Zhai, C., Tan, Q., Yue, D., Chen, D., Wang,
813 Z., Xie, S., Zeng, L., and Zhang, Y.: Daytime atmospheric oxidation capacity in four Chinese

814 megacities during the photochemically polluted season: a case study based on box model simulation,
815 *Atmos Chem Phys*, 19, 3493-3513, 10.5194/acp-19-3493-2019, 2019a.

816 Tan, Z. F., Lu, K. D., Jiang, M. Q., Su, R., Dong, H. B., Zeng, L. M., Xie, S. D., Tan, Q. W., and Zhang,
817 Y. H.: Exploring ozone pollution in Chengdu, southwestern China: A case study from radical chemistry
818 to O₃-VOC-NO_x sensitivity, *Sci Total Environ*, 636, 775-786, 10.1016/j.scitotenv.2018.04.286, 2018a.

819 Tan, Z. F., Lu, K. D., Dong, H. B., Hu, M., Li, X., Liu, Y. H., Lu, S. H., Shao, M., Su, R., Wang, H. C.,
820 Wu, Y. S., Wahner, A., and Zhang, Y. H.: Explicit diagnosis of the local ozone production rate and the
821 ozone-NO_x-VOC sensitivities, *Sci. Bull.*, 63, 1067-1076, 10.1016/j.scib.2018.07.001, 2018b.

822 Tan, Z. F., Lu, K. D., Hofzumahaus, A., Fuchs, H., Bohn, B., Holland, F., Liu, Y. H., Rohrer, F., Shao,
823 M., Sun, K., Wu, Y. S., Zeng, L. M., Zhang, Y. S., Zou, Q., Kiendler-Scharr, A., Wahner, A., and Zhang,
824 Y. H.: Experimental budgets of OH, HO₂, and RO₂ radicals and implications for ozone formation in the
825 Pearl River Delta in China 2014, *Atmos Chem Phys*, 19, 7129-7150, 10.5194/acp-19-7129-2019,
826 2019b.

827 Tan, Z. F., Fuchs, H., Lu, K. D., Hofzumahaus, A., Bohn, B., Broch, S., Dong, H. B., Gomm, S.,
828 Haseler, R., He, L. Y., Holland, F., Li, X., Liu, Y., Lu, S. H., Rohrer, F., Shao, M., Wang, B. L., Wang,
829 M., Wu, Y. S., Zeng, L. M., Zhang, Y. S., Wahner, A., and Zhang, Y. H.: Radical chemistry at a rural
830 site (Wangdu) in the North China Plain: observation and model calculations of OH, HO₂ and RO₂
831 radicals, *Atmos Chem Phys*, 17, 663-690, 10.5194/acp-17-663-2017, 2017.

832 Vaughan, S., Ingham, T., K. Whalley, L., Stone, D., Evans, M. J., Read, K. A., Lee, J. D., Moller, S. J.,
833 Carpenter, L. J., Lewis, A. C., Fleming, Z. L., and Heard, D. E.: Seasonal observations of OH and HO₂
834 in the remote tropical marine boundary layer, *Atmos. Chem. Phys.*, 12, 2149–2172, 10.5194/acp-12-
835 2149-2012, 2012.

836 Wang, F., Hu, R., Xie, P., Wang, Y., Chen, H., Zhang, G., and Liu, W.: Calibration source for OH
837 radical based on synchronous photolysis, *Acta Phys Sin-Ch Ed*, 69, 2020.

838 Wang, F. Y., Hu, R. Z., Chen, H., Xie, P. H., Wang, Y. H., Li, Z. Y., Jin, H. W., Liu, J. G., and Liu, W. Q.:
839 Development of a field system for measurement of tropospheric OH radical using laser-induced
840 fluorescence technique, *Opt. Express*, 27, A419-A435, 10.1364/oe.27.00a419, 2019.

841 Wang, J., Zhang, Y., Zhang, C., Wang, Y., Zhou, J., Whalley, L. K., Slater, E. J., Dyson, J. E., Xu, W.,
842 Cheng, P., Han, B., Wang, L., Yu, X., Wang, Y., Woodward-Massey, R., Lin, W., Zhao, W., Zeng, L.,
843 Ma, Z., Heard, D. E., and Ye, C.: Validating HONO as an Intermediate Tracer of the External Cycling
844 of Reactive Nitrogen in the Background Atmosphere, *Environ Sci Technol*, 10.1021/acs.est.2c06731,
845 2023.

846 Wang, T., Wei, X. L., Ding, A. J., Poon, C. N., Lam, K. S., Li, Y. S., Chan, L. Y., and Anson, M.:
847 Increasing surface ozone concentrations in the background atmosphere of Southern China, 1994-2007,
848 *Atmos Chem Phys*, 9, 6217-6227, 10.5194/acp-9-6217-2009, 2009.

849 Wang, Y., Hu, R., Xie, P., Chen, H., Wang, F., Liu, X., Liu, J., and Liu, W.: Measurement of
850 tropospheric HO₂ radical using fluorescence assay by gas expansion with low interferences, *J Environ
851 Sci (China)*, 99, 40-50, 10.1016/j.jes.2020.06.010, 2021.

852 Whalley, L. K., Furneaux, K. L., Goddard, A., Lee, J. D., Mahajan, A., Oetjen, H., Read, K. A., Kaaden,
853 N., Carpenter, L. J., Lewis, A. C., Plane, J. M. C., Saltzman, E. S., Wiedensohler, A., and Heard, D. E.:
854 The chemistry of OH and HO₂ radicals in the boundary layer over the tropical Atlantic Ocean, *Atmos
855 Chem Phys*, 10, 1555-1576, 10.5194/acp-10-1555-2010, 2010.

856 Woodward-Massey, R., Sommariva, R., Whalley, L. K., Cryer, D. R., Ingham, T., Bloss, W. J., Ball, S.
857 M., Lee, J. D., Reed, C. P., Crilley, L. R., Kramer, L. J., Bandy, B. J., Forster, G. L., Reeves, C. E.,

858 Monks, P. S., and Heard, D. E.: Radical chemistry at a UK coastal receptor site – Part 2: experimental
859 radical budgets and ozone production, *Atmos. Chem. Phys.*, 10.5194/acp-2022-213, 2022a.

860 Woodward-Massey, R., Sommariva, R., Whalley, L. K., Cryer, D. R., Ingham, T., Bloss, W. J., Ball, S.
861 M., Lee, J. D., Reed, C. P., Crilley, L. R., Kramer, L. J., Bandy, B. J., Forster, G. L., Reeves, C. E.,
862 Monks, P. S., and Heard, D. E.: Radical chemistry at a UK coastal receptor site – Part 1: observations
863 of OH, HO₂, RO₂, and OH reactivity and comparison to MCM model predictions, *Atmos. Chem. Phys.*,
864 10.5194/acp-2022-207, 2022b.

865 Xia, M., Wang, T., Wang, Z., Chen, Y., Peng, X., Huo, Y., Wang, W., Yuan, Q., Jiang, Y., Guo, H., Lau,
866 C., Leung, K., Yu, A., and Lee, S.: Pollution-Derived Br₂ Boosts Oxidation Power of the Coastal
867 Atmosphere, *Environ Sci Technol*, 10.1021/acs.est.2c02434, 2022.

868 Xia, S.-Y., Zhu, B., Wang, S.-X., Huang, X.-F., and He, L.-Y.: Spatial distribution and source
869 apportionment of peroxyacetyl nitrate (PAN) in a coastal region in southern China, *Atmos Environ.*, 260,
870 10.1016/j.atmosenv.2021.118553, 2021.

871 Xu, W., Ovadnevaite, J., Fossum, K. N., Lin, C., Huang, R.-J., Ceburnis, D., and O'Dowd, C.: Sea
872 spray as an obscured source for marine cloud nuclei, *Nature Geoscience*, 15, 282-286, 10.1038/s41561-
873 022-00917-2, 2022.

874 Yang, X., Lu, K., Ma, X., Gao, Y., Tan, Z., Wang, H., Chen, X., Li, X., Huang, X., He, L., Tang, M.,
875 Zhu, B., Chen, S., Dong, H., Zeng, L., and Zhang, Y.: Radical chemistry in the Pearl River Delta:
876 observations and modeling of OH and HO₂ radicals in Shenzhen in 2018, *Atmos Chem Phys*, 22,
877 12525-12542, 10.5194/acp-22-12525-2022, 2022a.

878 Yang, X., Lu, K., Ma, X., Gao, Y., Tan, Z., Wang, H., Chen, X., Li, X., Huang, X., He, L., Tang, M.,
879 Zhu, B., Chen, S., Dong, H., Zeng, L., and Zhang, Y.: Radical chemistry in the Pearl River Delta:
880 observations and 2 modeling of OH and HO₂ radicals in Shenzhen 2018, 10.5194/acp-2022-113, 2022b.

881 Yang, X., Lu, K., Ma, X., Liu, Y., Wang, H., Hu, R., Li, X., Lou, S., Chen, S., Dong, H., Wang, F.,
882 Wang, Y., Zhang, G., Li, S., Yang, S., Yang, Y., Kuang, C., Tan, Z., Chen, X., Qiu, P., Zeng, L., Xie, P.,
883 and Zhang, Y.: Observations and modeling of OH and HO₂ radicals in Chengdu, China in summer 2019,
884 *The Science of the total environment*, 772, 144829-144829, 10.1016/j.scitotenv.2020.144829, 2021a.

885 Yang, Y., Li, X., Zu, K., Lian, C., Chen, S., Dong, H., Feng, M., Liu, H., Liu, J., Lu, K., Lu, S., Ma, X.,
886 Song, D., Wang, W., Yang, S., Yang, X., Yu, X., Zhu, Y., Zeng, L., Tan, Q., and Zhang, Y.: Elucidating
887 the effect of HONO on O₃ pollution by a case study in southwest China, *Sci Total Environ.*, 756,
888 144127, 10.1016/j.scitotenv.2020.144127, 2021b.

889 Zeren, Y., Zhou, B., Zheng, Y., Jiang, F., Lyu, X., Xue, L., Wang, H., Liu, X., and Guo, H.: Does Ozone
890 Pollution Share the Same Formation Mechanisms in the Bay Areas of China?, *Environ Sci Technol*,
891 10.1021/acs.est.2c05126, 2022.

892 Zhang, G., Hu, R., Xie, P., Lou, S., Wang, F., Wang, Y., Qin, M., Li, X., Liu, X., Wang, Y., and Liu, W.:
893 Observation and simulation of HO_x radicals in an urban area in Shanghai, China, *Sci Total Environ.*,
894 810, 152275, 10.1016/j.scitotenv.2021.152275, 2022a.

895 Zhang, G., Hu, R., Xie, P., Lu, K., Lou, S., Liu, X., Li, X., Wang, F., Wang, Y., Yang, X., Cai, H., Wang,
896 Y., and Liu, W.: Intercomparison of OH radical measurement in a complex atmosphere in Chengdu,
897 China, *Sci Total Environ.*, 155924, 10.1016/j.scitotenv.2022.155924, 2022b.

898 Zhu, B., Huang, X.-F., Xia, S.-Y., Lin, L.-L., Cheng, Y., and He, L.-Y.: Biomass-burning emissions
899 could significantly enhance the atmospheric oxidizing capacity in continental air pollution, *Environ.*
900 *Pollut.*, 285, 10.1016/j.envpol.2021.117523, 2021.

901 Zhu, Y., Wang, Y., Zhou, X., Elshorbany, Y. F., Ye, C., Hayden, M., and Peters, A. J.: An investigation

902 into the chemistry of HONO in the marine boundary layer at Tudor Hill Marine Atmospheric
903 Observatory in Bermuda, *Atmos Chem Phys*, 22, 6327-6346, 10.5194/acp-22-6327-2022, 2022.
904 Zou, Z., Chen, Q., Xia, M., Yuan, Q., Chen, Y., Wang, Y., Xiong, E., Wang, Z., and Wang, T.: OH
905 measurements in the coastal atmosphere of South China: missing OH sinks in aged air masses,
906 *EGUsphere*, 2022, 1-47, 10.5194/egusphere-2022-854, 2022.
907